RZ 3874 (#ZUR1402-056) 02/28/2014
Physical Sciences 25 pages

Research Report

Contrast formation in Kelvin probe force microscopy of single π-conjugated molecules

Bruno Schuler,[1] Shi-Xia Liu,[2] Yan Geng,[2] Silvio Decurtins,[2] Gerhard Meyer,[1] and Leo Gross[1]

[1]IBM Research – Zurich, 8803 Rüschlikon, Switzerland

[2]Departement für Chemie und Biochemie, Universität Bern,
Freiestrasse 3, 3012 Bern, Switzerland

Contrast formation in Kelvin probe force microscopy of single π-conjugated molecules

Bruno Schuler,[*,†] Shi-Xia Liu,[*,‡] Yan Geng,[‡] Silvio Decurtins,[‡] Gerhard Meyer,[†] and Leo Gross[†]

IBM Research – Zurich, Säumerstrasse 4, 8803 Rüschlikon, Switzerland, and Departement für Chemie und Biochemie, Universität Bern, Freiestrasse 3, 3012 Bern, Switzerland

E-mail: bsc@zurich.ibm.com; liu@dcb.unibe.ch

Abstract

We report on the contrast formation in the local contact potential difference (LCPD) measured by Kelvin probe force microscopy (KPFM) on single charge-transfer complexes (CTCs) on a NaCl bilayer on Cu(111). At different tip heights, we found quantitatively different LCPD contrasts that characterize different properties of the molecule. In the small distance regime, the tip penetrates the electron density of the molecule, and the contrast is related to the size and topography of the electron shell of the molecule. For larger distances, the LCPD contrast corresponds to the electrostatic field above the molecule. However, in the medium-distance regime, i.e., for tip heights similar to the size of the molecule, the non-spherical distribution of π- and σ-electrons often conceals the effect of the partial charges within the molecule. Only for large distances does the LCPD map converge towards the simple field of a dipole for a polar molecule.

*To whom correspondence should be addressed

†IBM Research – Zurich, Säumerstrasse 4, 8803 Rüschlikon, Switzerland

‡Departement für Chemie und Biochemie, Universität Bern, Freiestrasse 3, 3012 Bern, Switzerland

Keywords

Kelvin probe force microscopy (KPFM), noncontact atomic force microscopy (NC-AFM), charge-transfer complex (CTC), donor-acceptor molecules, charge distribution

Main text

Measuring and understanding the detailed charge distribution in individual charge-transfer complexes (CTCs) are of particular interest because of their application in molecular electronics[1–4] and organic photovoltaics.[5] Using different scanning probe methods, the properties of individual molecules can be mapped with submolecular resolution: with scanning tunneling microscopy (STM), the molecular frontier orbitals can be probed[6,7] and for a polar molecule the spatial separation of the lowest unoccupied molecular orbital (LUMO) and the highest occupied molecular orbital (HOMO) has been shown.[8] Using noncontact atomic force microscopy (NC-AFM),[9] the atoms and bonds within a molecule can be imaged[10] and the adsorption geometry can be obtained.[11,12] Finally, by Kelvin probe force microscopy (KPFM),[13] one measures the local contact potential difference (LCPD), which yields information about the distribution of charges. With KPFM, charge sensitivity has been demonstrated on single atoms,[14] defects,[15–18] surfaces,[18–22] and also on molecules.[23–25] However,

the underlying contrast mechanism of KPFM at the atomic scale and the interpretation of atomically resolved LCPD maps are still under debate and are also tackled by recent theoretical studies.[26,27]

Here we investigate individual covalently linked donor–acceptor (polar) and acceptor–donor–acceptor (bipolar) CTCs.[28,29] Thereby, the molecules under investigation were designed specifically as compactly fused donor–acceptor and donor–acceptor–donor entities. We make use of STM and AFM to determine and switch the molecular adsorption geometry and investigate its effect on the LCPD. Furthermore, we compare our measurements with calculations of the electrostatic field above the molecule. As a function of tip height, we find different molecular properties that determine the LCPD maps. Our results demonstrate that the information obtained by KPFM goes even beyond the determination of partial charges within the molecule.

The experiments were performed with a combined STM/AFM based on a qPlus tuning fork design[30] operated in the frequency-modulation mode[31] (oscillation amplitude = 0.5 Å) under ultrahigh-vacuum and low temperature (T = 5 K) conditions. The bias voltage was applied to the sample. As substrate, two-monolayer thick (100)-oriented NaCl islands on Cu(111) [NaCl(2ML)/Cu(111)] were grown to electronically decouple the molecules from metal states. We investigated different CTCs with varying types [pyrazine (PYZ) or thiadiazole (TDZ)] and numbers (one or two) of acceptor components and a common tetrathiafulvalene (TTF) donor. The CTC molecules were thermally evaporated onto the cold sample. As tip, we used a focused-ion-beam-cut PtIr wire, which was repeatedly indented into the Cu substrate. To functionalize such a Cu-coated tip, a CO molecule was picked up by vertical manipulation.

In Fig. 1(a), the structure of the bipolar CTC TTF-PYZ_2 is shown. TTF-PYZ_2 on NaCl(2ML)/Cu(111) has two different conformational states (isomers) called 'up' and 'down'

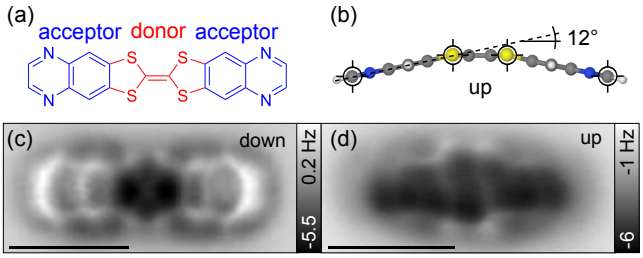

Figure 1: **TTF-PYZ_2 AFM (a)** Model of TTF-PYZ_2 with the donor part in red and the acceptor part in blue. **(b)** Side-view on the relaxed boat geometry of TTF-PYZ_2 in the 'up' conformation with the dihedral angle of $\theta = 12\,^\circ$ indicated. Color code: H: white, C: gray, N: blue, S: yellow. **(c,d)** Constant-height AFM images of TTF-PYZ_2 in the 'down' (c) and 'up' (d) conformation with a CO tip. Scale bars: 10 Å.

with different adsorption sites (see Fig. S7). The chemical structure of the two states can be identified by constant-height AFM imaging of the molecule with a CO tip [see Fig. 1(c,d)].[10,32] In the 'down' state, the TTF part in the center is closer to the substrate than the molecule's ends, which therefore appear more pronounced and brighter than the central part in Fig. 1(c). In contrast, for the 'up' state [Fig. 1(d)], the TTF part with its clearly visible four S atoms is sticking out. The Δf contrast difference between the outer and the center part is a consequence of the non-planar adsorption geometry and the high sensitivity of the short-range repulsive forces (Pauli repulsion) to changes of the tip–molecule distance.[11,12]

To corroborate our interpretation of the molecular geometry, we performed density functional theory (DFT) calculations of the free TTF-PYZ_2 molecule with the highly optimized plane–wave code `CPMD`. We used the Perdew-Burke-Ernzerhof (PBE) exchange-correlation functional, *ab initio* norm-conserving pseudopotentials and added semiempirical van der Waals (vdW) corrections.[33] In the optimized geometry, we find indeed a boat-type geometry with a dihedral angle of $\theta = 12°$ [see Fig. 1(b)]. This is very close to $\theta = 13.5°$ for bare TTF measured by gas electron diffraction.[34] The

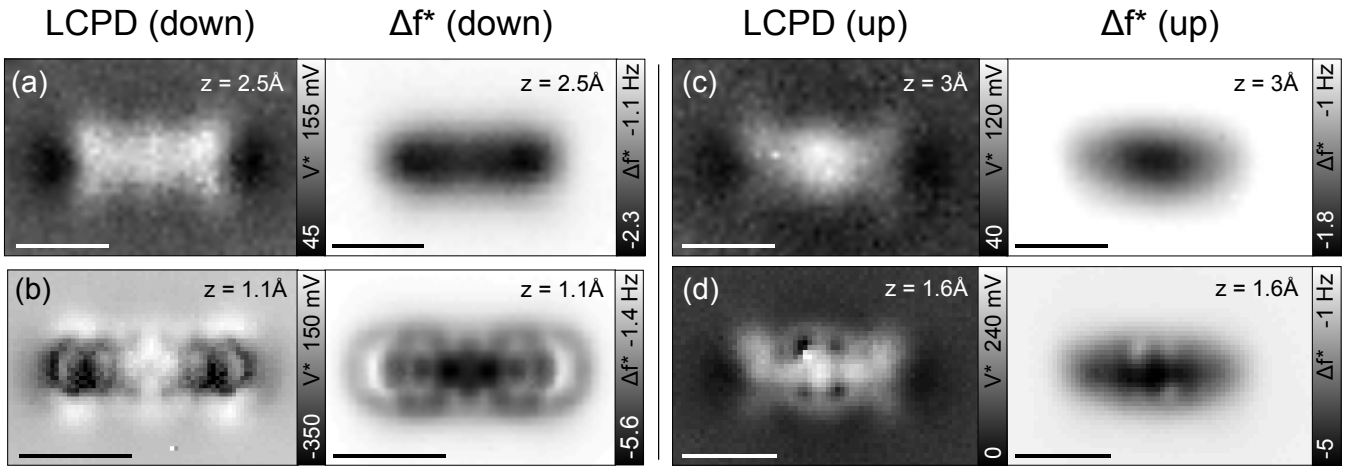

Figure 2: **TTF-PYZ$_2$ KPFM (a,b)/(c,d)** LCPD (V^*) maps of TTF-PYZ$_2$ in the 'down'/'up' conformation at different heights z with a CO tip and the corresponding AFM maps at compensated LCPD (Δf^*). The heights are given with respect to an STM set point of ($I = 2\,\mathrm{pA}$, $V = 0.2\,\mathrm{V}$) over the substrate. Scale bars: 10 Å.

calculated energy profile for the bending into a planar geometry is very shallow ($\Delta E \approx 4\,\mathrm{mV}$). This high flexibility[35] allows an easy transition between the 'up' and the 'down' boat state.

To gain insights into the charge state and charge distribution of the CTC and the effect of conformation on the aforementioned, we acquired maps of the LCPD above the molecule implemented by force-bias spectroscopy $\Delta f(V)$.[14,21,24,36] From the individual parabolic $\Delta f(V)$ spectra, the peak voltage and the peak frequency shift (V^*,Δf^*) are extracted. This voltage V^* corresponds to the LCPD divided by the elementary charge. Maps of V^*, called LCPD maps in the following, are obtained by recording $\Delta f(V)$ spectra point by point in constant-height mode on a lateral grid with a typical acquisition time of 15 h.

In Fig. 2, LCPD maps of TTF-PYZ$_2$ and the corresponding maps of the LCPD-compensated frequency shift Δf^* are depicted. A CO tip has been used to explore also the small-distance regime. At moderate distance, the LCPD images recorded with a CO tip [Fig. 2(a,c)] resemble those obtained with a Cu tip (see Fig. S1). In this regime we observe for both conformations ('up' and 'down') a similar LCPD contrast. Interestingly, the LCPD is increased at the positively charged donor as well as at the negatively charged acceptor sites as compared to the bare substrate. To the left and right of the molecule, the LCPD is decreased. This contrast contradicts the simple interpretation of LCPD maps (neglecting higher-order multipoles) of a positive/negative charge giving rise to a decreased/increased local work function and thus a decreased/increased LCPD. These findings are not specific to this particular molecule, but are also observed for TTF-TDZ$_2$ (see Fig. S6).

With the CO tip, we can access the small-distance regime where Pauli repulsion sets in, and here the LCPD changes abruptly and significantly [Fig. 2(b,d)]. At positions of repulsive interaction, the LCPD is decreased by several 100 mV. This LCPD decrease has the same high spatial localization as the repulsive Δf^* signal and sets in at the same imaging height, suggesting a correlation between Δf^* and the LCPD channel. This can be clearly seen by comparing Δf^* and LCPD contrast for both conformations, for example, considering the four bright Δf^* spots and the four dark LCPD spots in Fig. 2(d). The LCPD decrease at small distances can be explained by a local penetration of the tip in areas of significant electron density, which leaves the molecule's atomic cores partially unshielded. Consistently, the immersion of the tip into the extended π-orbitals leads to the repulsive Pauli interaction.

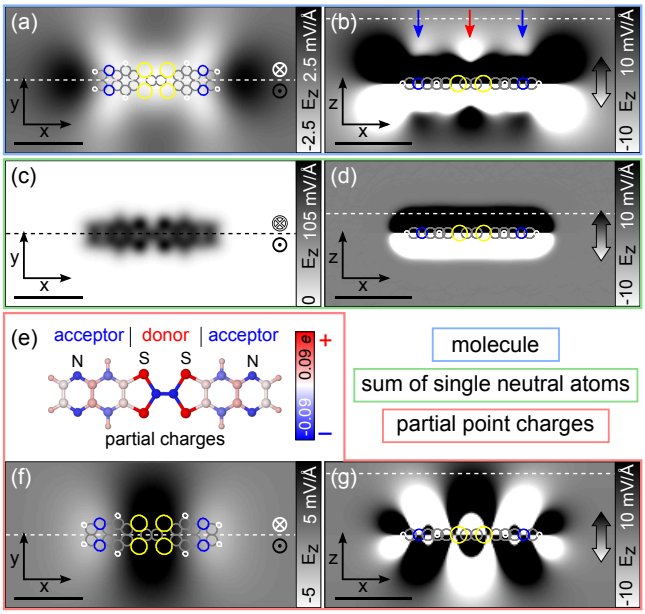

Figure 3: **TTF-PYZ$_2$ theory (a)** Calculated z-component of the electrostatic field (E_z) of the flat TTF-PYZ$_2$ at 8.6 Å away from the molecular plane [dashed line in (b)]. **(b)** E_z in the x-z plane through the molecule's center [dashed line in (a)]. Blue/red arrows indicate acceptor/donor positions. **(c)** Calculated E_z by assuming a set of non-interacting (spherical symmetric) neutral atoms in the TTF-PYZ$_2$ arrangement, at 2.5 Å away from the molecular plane [dashed line in (d)]. **(d)** E_z in the x-z plane at the dashed line in (c). **(e)** DFT-calculated partial charges of TTF-PYZ$_2$ by real-space integration. **(f)** Calculated E_z generated by the partial point charges of TTF-PYZ$_2$ at 8.6 Å away from the molecular plane [dashed line in (g)]. **(g)** E_z in the x-z plane at the dashed line in (f). In (a,b,d,f,g) the molecule structure is overlaid (color code: H: white, C: gray, N: blue, S: yellow). Scale bars: 10 Å.

To understand the apparently conflicting contrast of the measured and expected LCPD, we calculated the electrostatic field and partial atomic charges of the free, planar TTF-PYZ$_2$ molecule. The use of the planar instead of the boat geometry for these calculations is justified at larger distances because of the small differences of the LCPD and the Δf^* channel for both conformations at moderate height. The insulating NaCl layer provides an electronic decoupling and prevents hybridization and partial charge transfer with metal states. Since the molecule is neutral, we do not expect strong modifications of the surface dipoles as on metals. This allows us to compare the measurements on NaCl with calculations of the free molecule. The measured V^* contrast at the atomic scale qualitatively reflects the z-component of the electrostatic field (E_z) created by the sample.[18,24] A quantitative comparison is challenging due to the different work functions of the mesoscopic tip and sample surfaces and the resulting averaging effects.[14] Fig. 3(a) shows E_z in the x-y plane 8.6 Å above the molecule.[37] In comparison with Fig. 2(a,c), the measured LCPD contrast is well reproduced by E_z showing only slight deviations that can be attributed to the nonplanar geometry.

In the following, we will describe which aspect of the molecular charge distribution will contribute in which way to the molecular E-field. In first order, the charge distribution of the molecule can be described by a set of single non-interacting neutral atoms with spherical symmetric charge distributions. The E_z-field from this charge distribution is displayed in Fig. 3(c,d). We observe a short-ranged field that points away from the molecule in regions of significant electron density and is zero in the far field. For small distances this effect is predominant and resembles the total electron density that is also probed by the Δf^* signal. However, it cannot be decisive for medium and larger distances. A second major component is the E-field produced by the partial atomic charges resulting from polarization of bonds. This field has considerable multipole moments and can have large contributions in the medium- and large-distance regimes. In Fig. 3(e), the partial atomic charges of the bipolar TTF-PYZ$_2$ molecule are illustrated. As expected, the N heteroatoms of PYZ act as electron acceptors with a net electron excess of 0.07 e, whereas electrons are depleted at the TTF donor. The corresponding E-field generated by these point charges is shown in Fig. 3(f,g). Note that E_z beyond the small-distance regime [Fig. 3(f)] resembles a field

of two opposing dipoles $(-+\,+-)$ in consensus with the expected behavior of the bipolar molecule. Apparently, the sum of the fields generated by the spherical symmetric electron distribution and partial atomic charges does not result in the calculated (and measured) molecular E-field. The missing crucial factor, not considered so far, is the complex three-dimensional distribution of the electron density. In the case of the bipolar TTF-PYZ_2 molecule, this effect even leads to an inversion of the E_z contrast above donor and acceptor positions [compare Fig. 3(a,b) with Fig. 3(f,g)]. The resulting E-field, which is in agreement with the experiment, is reminiscent of two opposing dipoles in the orientation $(+--+)$ although the dipoles in the molecule are oriented $(-+\,+-)$. This finding demonstrates that the LCPD image of a molecule cannot be broken down into an assembly of partial point charges located at the atom positions, but that the complex electron distribution in space has to be considered. Note that this effect of the electron distribution can be elegantly accounted for when measuring the charge transfer. However, this is possible only for stable molecular conformations with different charge distributions by looking at the difference of their LCPD maps.[24]

To investigate the far-distance regime, we also examined the polar TTF-TDZ molecule, depicted in Fig. 4(a), which has a nonvanishing lateral dipole moment ($p = 4.2\,\mathrm{D}$). For TTF-TDZ, the measured LCPD shown in Fig. 4(c) is also in very good qualitative agreement with E_z [c.f. Fig. 4(d)]. Although the E-field at medium distance is again more complex than its lowest-order multipole moment, it contains large contributions from the molecular dipole. In the far field, the calculated E-field converges to a simple dipole field [see Fig. 4(e)] in agreement with the expected behavior of a donor-acceptor molecule. Note that at these large distances the LCPD signal from the molecule is below our experimental limit of detection.

In summary, we investigated the bipolar CTCs TTF-PYZ_2 and TTF-TDZ_2 and the polar CTC TTF-TDZ on NaCl(2ML)/Cu(111)

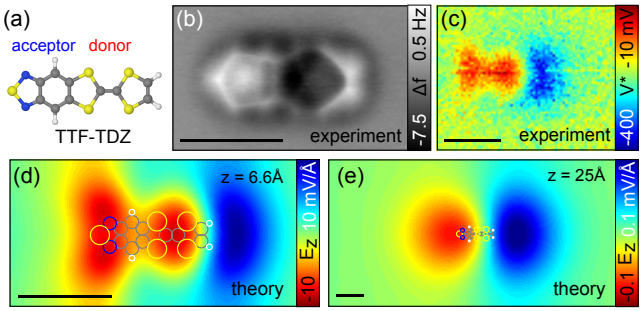

Figure 4: **Polar TTF-TDZ** **(a)** Model of TTF-TDZ. Color code: H:white, C:gray, N:blue, S:yellow. **(b)** Constant-height AFM image of TTF-TDZ with a CO tip. Similarly to TTF-TDZ_2 and TTF-PYZ_2 also TTF-TDZ has boat-like geometry. **(c)** LCPD (V^*) map of TTF-TDZ using a Cu tip. **(d,e)** Calculated z-component of the electrostatic field (E_z) at different heights z with a molecule model overlaid. In (e) the far field of the molecular dipole is visible. Scale bars: 10 Å.

using STM, AFM and KPFM. Both bipolar molecules show two conformational states 'up' and 'down', that were identified by AFM with CO-functionalized tips and corroborated by DFT. In KPFM, three main distance regimes were identified that exhibit quantitatively different contrast and are related to different aspects of the charge distribution within the molecule: At distances much larger than the molecule dimensions, the LCPD contrast resembles the electrostatic far-field with predominant contributions of the molecular electric monopole (net charge) and dipole. At distances similar to the molecule dimensions, the LCPD contrast corresponds to the electrostatic field with predominant contributions from higher-order multipoles caused by partial atomic charges and the complex 3D electron distribution. At very small distances, which can be explored with a CO-terminated tip, the tip penetrates the electron density of the molecule. As a result, the molecule's nuclei are left partially unshielded, and the LCPD shows a strong decrease of several 100 mV at positions of high total electron density, in agreement with the occurrence of repulsive Pauli interaction. Only in this small distance regime do the tip and the adsorption geometry of the molecule

play an important role for the LCPD measured.

Acknowledgement The authors thank N. Moll for help with running the DFT codes and R. Allenspach for comments on the manuscript. B.S., G.M. and L.G. acknowledge financial support from the ERC Advanced Grant CEMAS and EU project PAMS. S.L., Y.G. and S.D. acknowledge support from the Swiss National Science Foundation (grant no. 200021-147143).

Supporting Information Available: Additional distance-dependent LCPD maps, individual spectra, calculations of the electrostatic field, and discussion of adsorption sites, synthesis and spectroscopic characterization. This material is available free of charge via the Internet at `http://pubs.acs.org/`.

Notes and References

(1) Aviram, A.; Ratner, M. A. *Chem. Phys. Lett.* **1974**, *29*, 277–283.

(2) Joachim, C.; Gimzewski, J.; Aviram, A. *Nature* **2000**, *408*, 541–548.

(3) Elbing, M.; Ochs, R.; Koentopp, M.; Fischer, M.; von Hänisch, C.; Weigend, F.; Evers, F.; Weber, H. B.; Mayor, M. *Proc. Natl. Acad. Sci. U.S.A.* **2005**, *102*, 8815–8820.

(4) Pfattner, R.; Pavlica, E.; Jaggi, M.; Liu, S.-X.; Decurtins, S.; Bratina, G.; Veciana, J.; Mas-Torrent, M.; Rovira, C. *J. Mater. Chem. C* **2013**, *1*, 3985–3988.

(5) Sariciftci, N.; Wudl, F.; Heeger, A.; Maggini, M.; Scorrano, G.; Prato, M.; Bourassa, J.; Ford, P. *Chem. Phys. Lett.* **1995**, *247*, 510–514.

(6) Repp, J.; Meyer, G.; Stojković, S. M.; Gourdon, A.; Joachim, C. *Phys. Rev. Lett.* **2005**, *94*, 026803.

(7) Soe, W.-H.; Manzano, C.; De Sarkar, A.; Chandrasekhar, N.; Joachim, C. *Phys. Rev. Lett.* **2009**, *102*, 176102.

(8) Tao, C.; Sun, J.; Zhang, X.; Yamachika, R.; Wegner, D.; Bahri, Y.; Samsonidze, G.; Cohen, M. L.; Louie, S. G.; Tilley, T. D.; Segalman, R. A.; Crommie, M. F. *Nano Lett.* **2009**, *9*, 3963–3967.

(9) Morita, S.; Wiesendanger, R.; Meyer, E. A. *Noncontact atomic force microscopy*; Springer, 2002; Vol. 1.

(10) Gross, L.; Mohn, F.; Moll, N.; Liljeroth, P.; Meyer, G. *Science* **2009**, *325*, 1110–1114.

(11) Pavliček, N.; Fleury, B.; Neu, M.; Niedenführ, J.; Herranz-Lancho, C.; Ruben, M.; Repp, J. *Phys. Rev. Lett.* **2012**, *108*, 086101.

(12) Schuler, B.; Liu, W.; Tkatchenko, A.; Moll, N.; Meyer, G.; Mistry, A.; Fox, D.; Gross, L. *Phys. Rev. Lett.* **2013**, *111*, 106103.

(13) Nonnenmacher, M.; O'Boyle, M. P.; Wickramasinghe, H. K. *Appl. Phys. Lett.* **1991**, *58*, 2921–2923.

(14) Gross, L.; Mohn, F.; Liljeroth, P.; Repp, J.; Giessibl, F. J.; Meyer, G. *Science* **2009**, *324*, 1428–1431.

(15) Barth, C.; Henry, C. R. *Phys. Rev. Lett.* **2007**, *98*, 136804.

(16) König, T.; Simon, G. H.; Rust, H.-P.; Pacchioni, G.; Heyde, M.; Freund, H.-J. *J. Am. Chem. Soc.* **2009**, *131*, 17544.

(17) Pawlak, R.; Glatzel, T.; Pichot, V.; Schmidlin, L.; Kawai, S.; Fremy, S.; Spitzer, D.; Meyer, E. *Nano Lett.* **2013**, *13*, 5803–5807.

(18) Gross, L.; Schuler, B.; Mohn, F.; Moll, N.; Scivetti, I.; Kotsis, K.; Persson, M.; Meyer, G. *(in preparation)* **2014**,

(19) Bocquet, F.; Nony, L.; Loppacher, C.; Glatzel, T. *Phys. Rev. B* **2008**, *78*, 035410.

(20) Enevoldsen, G. H.; Glatzel, T.; Christensen, M. C.; Lauritsen, J. V.; Besenbacher, F. *Phys. Rev. Lett.* **2008**, *100*, 236104.

(21) Sadewasser, S.; Jelinek, P.; Fang, C.-K.; Custance, O.; Yamada, Y.; Sugimoto, Y.; Abe, M.; Morita, S. *Phys. Rev. Lett.* **2009**, *103*, 266103.

(22) Yurtsever, A.; Sugimoto, Y.; Fukumoto, M.; Abe, M.; Morita, S. *Appl. Phys. Lett.* **2012**, *101*, 083119.

(23) Leoni, T.; Guillermet, O.; Walch, H.; Langlais, V.; Scheuermann, A.; Bonvoisin, J.; Gauthier, S. *Phys. Rev. Lett.* **2011**, *106*, 216103.

(24) Mohn, F.; Gross, L.; Moll, N.; Meyer, G. *Nature Nanotech.* **2012**, *7*, 227–231.

(25) Kawai, S.; Sadeghi, A.; Feng, X.; Lifen, P.; Pawlak, R.; Glatzel, T.; Willand, A.; Orita, A.; Otera, J.; Goedecker, S.; Meyer, E. *ACS Nano* **2013**, *7*, 9098–9105.

(26) Sadeghi, A.; Baratoff, A.; Ghasemi, S. A.; Goedecker, S.; Glatzel, T.; Kawai, S.; Meyer, E. *Phys. Rev. B* **2012**, *86*, 075407.

(27) Bocquet, F.; Nony, L.; Loppacher, C. *Phys. Rev. B* **2011**, *83*, 035411.

(28) Pop, F.; Amacher, A.; Avarvari, N.; Ding, J.; Daku, L. M. L.; Hauser, A.; Koch, M.; Hauser, J.; Liu, S.-X.; Decurtins, S. *Chem. Eur. J.* **2013**, *19*, 2504–2514.

(29) Amacher, A.; Luo, H.; Liu, Z.; Bircher, M.; Cascella, M.; Hauser, J.; Decurtins, S.; Zhang, D.; Liu, S.-X. *RSC Adv.* **2014**, *4*, 2873–2878.

(30) Giessibl, F. J. *Appl. Phys. Lett.* **1998**, *73*, 3956–3958.

(31) Albrecht, T. R.; Grütter, P.; Horne, D.; Rugar, D. *J. Appl. Phys.* **1991**, *69*, 668–673.

(32) Mohn, F.; Schuler, B.; Gross, L.; Meyer, G. *Appl. Phys. Lett.* **2013**, *102*, 073109.

(33) Perdew, J.; Burke, K.; Ernzerhof, M. *Phys. Rev. Lett.* **1996**, *77*, 3865–3868.

(34) Hargittai, I.; Brunvoll, J.; Kolonits, M.; Khodorkovsky, V. *J. Mol. Struct.* **1994**, *317*, 273–277.

(35) Viruela, R.; Viruela, P.; Pou-Amérigo, R.; Ortí, E. *Synth. Met.* **1999**, *103*, 1991–1992.

(36) Burke, S.; LeDue, J.; Miyahara, Y.; Topple, J.; Fostner, S.; Grütter, P. *Nanotechnology* **2009**, *20*, 264012.

(37) The height was adjusted to reproduce the measured LCPD contrast in Fig. 2(a,c). But as seen in Fig. S3, the contrast of E_z beyond $z \approx 5$Å qualitatively no longer changes significantly.

Contrast formation in Kelvin probe force microscopy of single π-conjugated molecules

SUPPORTING INFORMATION (SI)

Bruno Schuler,*,† Shi-Xia Liu,*,‡ Yan Geng,‡ Silvio Decurtins,‡ Gerhard Meyer,† and Leo Gross†

IBM Research – Zurich, Säumerstrasse 4, 8803 Rüschlikon, Switzerland, and Departement für Chemie und Biochemie, Universität Bern, Freiestrasse 3, 3012 Bern, Switzerland

E-mail: bsc@zurich.ibm.com; liu@dcb.unibe.ch

KPFM distance dependence

In Fig. S1, LCPD and the corresponding Δf^*maps of TTF-PYZ_2 in the 'down' conformation are shown for different heights z recorded with a Cu and CO tip. In the intermediate distance regime that can be accessed by Cu and CO tips [Fig. S1(a-d)], the LCPD contrast is in good agreement with the electrostatic field [see Fig. S3(d-f)] at a given height generated by the total charge distribution within the molecule. Qualitatively, the KPFM contrast obtained with a Cu and a CO tip is very similar. Note, however, that the imaging heights of a Cu and a CO tip are different at a certain STM set point. In the close distance regime [Fig. S1(e,f)], where Pauli repulsion is observed in the Δf^*channel and which was only accessible with a CO-functionalized tip, the LCPD is drastically decreased by several 100 mV at positions of

*To whom correspondence should be addressed
†IBM Research – Zurich, Säumerstrasse 4, 8803 Rüschlikon, Switzerland
‡Departement für Chemie und Biochemie, Universität Bern, Freiestrasse 3, 3012 Bern, Switzerland

repulsive interaction. This effect results from a local penetration of the tip probe into the molecule electron density. At this distance, the positive atomic cores are not completely compensated by the negative charge of the electron density. Hence, the LCPD drops in regions where the electron density is largest, i.e., in the close-distance regime the LCPD signal is dominated by the total electron density. In Fig. S2(a-c) individual $\Delta f(V)$ spectra, extracted from the measurements depicted in Fig. S1(b-f), are shown. The position (*i*) corresponds to the left C-C bond, position (*ii*) is above the left ring of TTF and the position (*iii*) at the bare NaCl substrate. Note that for all measurement heights and positions we did neither observe significant deviations from the parabolic $\Delta f(V)$ dependence nor correlations to the tunneling current [shown in Fig. S2(d-f)].

Electrostatic field

In Fig. S3, the height dependence of the z-component of the electrostatic field (E_z) of TTF-PYZ_2 is shown. In the regime up to about 5 Å, E_z is subject to qualitative contrast changes. Further away the contrast persists qualitatively, but changes in its strength. Note that this E_z contrast is reminiscent of two opposing dipoles in the order $(+\,-)$ and $(-\,+)$. But in this CTC molecule, the sequence is exactly opposite: acceptor $(-)$ to the left, donor $(++)$ in the center and acceptor $(-)$ to the right, which is also corroborated by the calculated partial charges of the donor and acceptor components (see Fig. 3). This again demonstrates that E_z and hence the LCPD cannot be translated directly into the partial charge at a certain position.

It should be noted that the simplified model used shows very good agreement with the experiments, although it neglects all influences of the tip and sample. However, quantitatively there might be influences of both tip and sample. For example tip dipoles or the electrostatic field of the ionic substrate[3] might induce small atom displacements in the molecule or

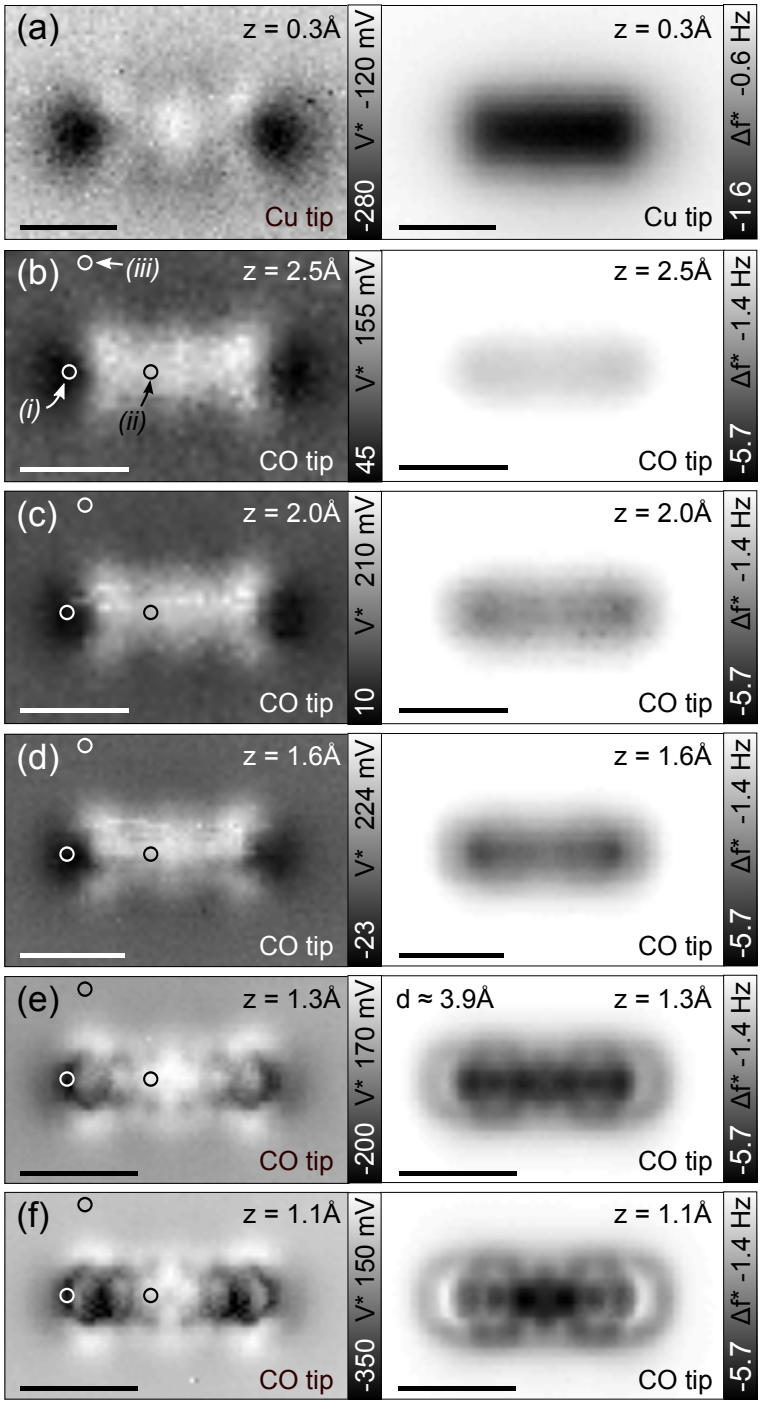

Figure S1: **KPFM TTF-PYZ$_2$.** **(a)/(b-f)** LCPD (V^*) maps of TTF-PYZ$_2$ in the 'down' conformation at different heights z with a Cu/CO tip and the corresponding AFM maps at compensated LCPD (Δf^*). In measurements (b-f) the same CO tip was used. The heights are given with respect to an STM set point of ($I = 2\,\mathrm{pA}$, $V = 0.2\,\mathrm{V}$) over the substrate. In (e) $\Delta f^* \approx \Delta f_{\mathrm{min}}$ at the center of the carbon rings and the distance between the oxygen atom of the CO tip and the molecular plane can be estimated to be $d \approx 3.9\,\text{Å}$.[1,2] Individual $\Delta f(V)$ spectra at the three positions $(i) - (iii)$ are shown in Fig. S2a-c. Scale bars: 10 Å.

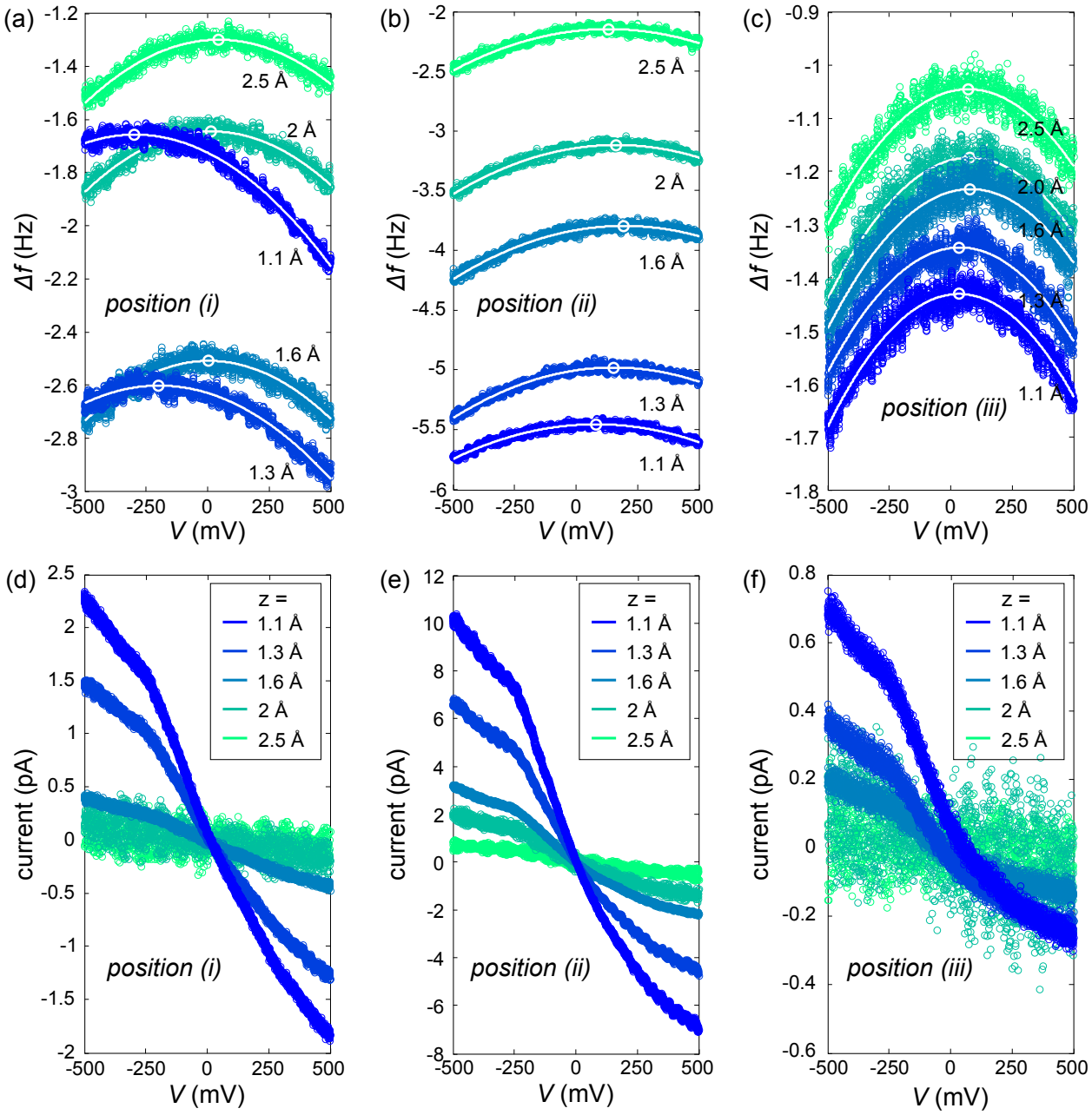

Figure S2: **Individual $\Delta f(V)$ and $I(V)$ spectra.** **(a-c)** Individual $\Delta f(V)$ spectra at different heights $z = 1.1 - 2.5$ Å extracted from the KPFM measurements and the positions $(i) - (iii)$ indicated in Fig. S1b-f. For all measurement heights and positions there were no significant deviations from the parabolic $\Delta f(V)$ dependence observed. **(d-f)** Tunneling current recorded simultaneously with the Δf signal shown in (a-c), respectively.

polarize the molecule.

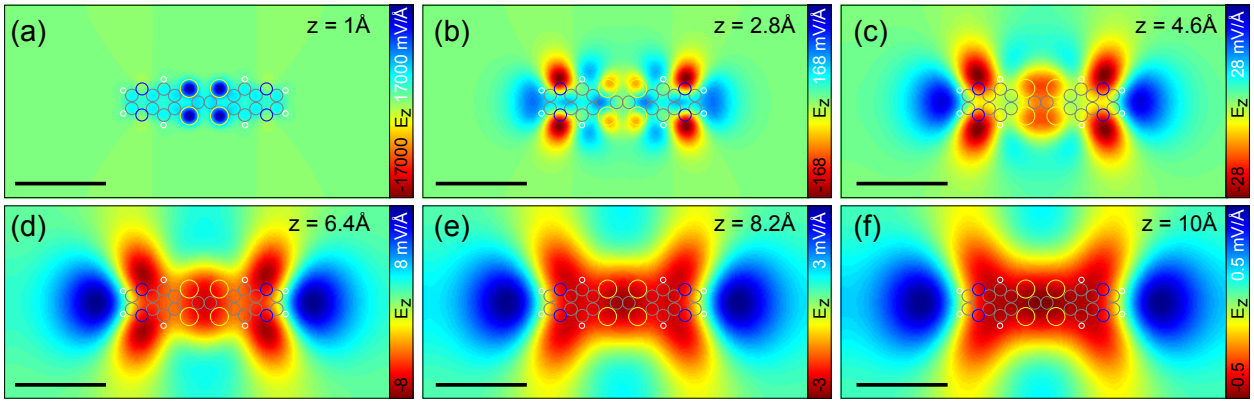

Figure S3: **Electrostatic field of TTF-PYZ$_2$.** **(a-f)** Calculated z-component of the electrostatic field (E_z) at different (equidistant) heights z with the molecule model overlaid. Scale bars: 10 Å.

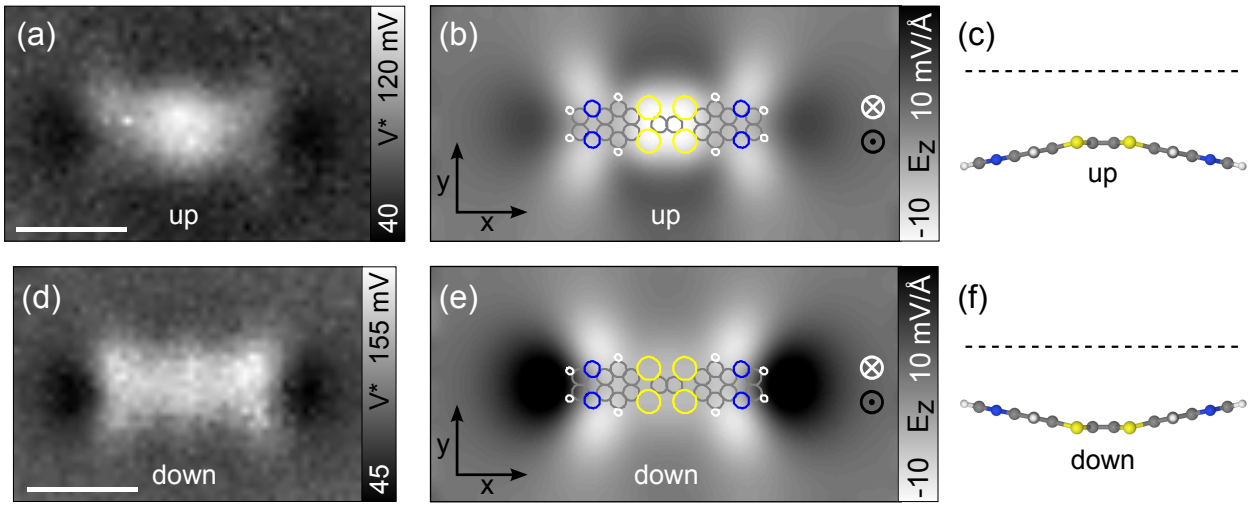

Figure S4: **Electrostatic field of bent TTF-PYZ$_2$.** **(a/d)** LCPD map of TTF-PYZ$_2$ in the 'up'/'down' conformation. **(b/e)** E$_z$-field in the x-y plane for the TTF-PYZ$_2$ molecule in the 'up'/'down' conformation (z = 7 Å). **(c/f)** Molecule model in the 'up'/'down' conformation and the image planes of (b) and (e) indicated by the dashed lines. Scale bars: 10 Å.

In Fig. S4(b,e) the electrostatic field of the molecule in the bent geometry is shown. In comparison with the measurements of the 'up' and 'down' conformation [Fig. S4(a,d)] even subtle features like the brighter center of the 'up' conformation and the darker ends of the 'down' conformation are visible. Qualitatively, however, both 'up' and 'down' agree with the

calculated E-field in the planar geometry (as shown in the manuscript).

We also examined the intramolecular charge-transfer transition (ICT) of the charge-transfer complexes, where an electron is excited from the HOMO localized on the TTF to the LUMO localized on the acceptor (see also Section Spectroscopic Characterization). In Fig. S5, the calculated E_z of TTF-PYZ$_2$ in this excited state is shown. Strikingly, the E-field in the excited state looks qualitatively very different compared to the E-field in the ground state (c.f. Fig. S3). After the ICT, the E-field from about $z \approx 4\,\text{Å}$ on clearly resembles a field that can be described by two opposing dipoles in the sequence $(-++-)$, as expected after donation of one electron from the center to the molecule's ends. In this case, the large partial charges (on the order of $1e$) are the predominating effect for the E-field contrast. Note that the E-field strength in the medium distance regime is approximately by a factor of 5 larger for the molecule after the ICT than the the molecule in the ground state [compare Fig. S3(d-f) with Fig. S5(d-f)]. We were not able to measure the molecule in the ICT state by scanning probe microscopy, because of the short lifetime (in the range of ps) of the excitation.

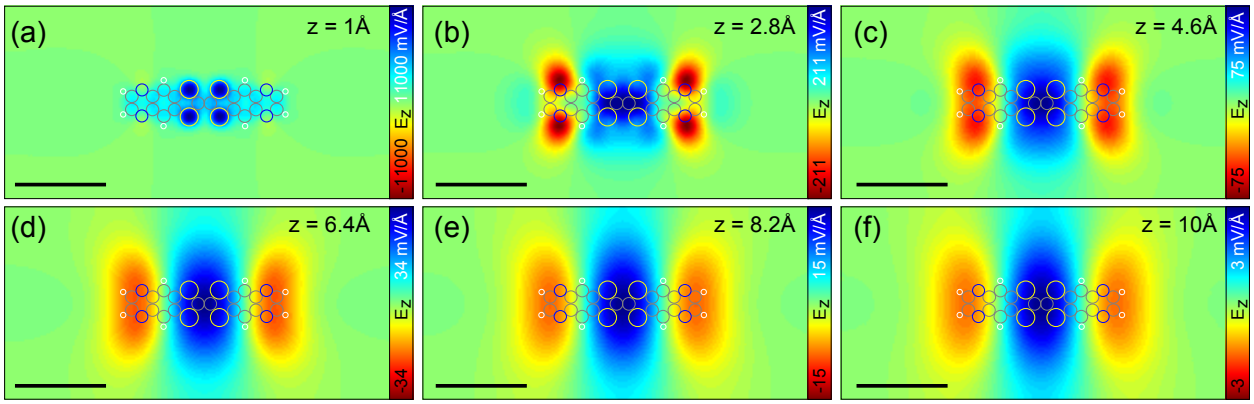

Figure S5: **Electrostatic field of TTF-PYZ$_2$ after the intramolecular charge transfer transition (ICT). (a-f)** Calculated z-component of the electrostatic field (E_z) at different (equidistant) heights z of TTF-PYZ$_2$ after the transition of one electron from the HOMO to the LUMO (ICT) with the molecule model overlaid. The simplification has been made that the geometry of the charge-transfer state is the same as in the ground state. Note that the scales are slightly different compared to Fig. S3. Scale bars: 10 Å.

Bipolar TTF-TDZ$_2$

In addition to the polar TTF-TDZ and bipolar TTF-PYZ$_2$ molecule, we also examined the bipolar TTF-TDZ$_2$ molecule. Fig. S6(a,b) show STM topographies of TTF-TDZ$_2$ on NaCl(2ML)/Cu(111). Analogously to TTF-PYZ$_2$, also TTF-TDZ$_2$ has two different conformational states, 'up' and 'down', with different adsorption sites as shown in the AFM images with a CO tip in Fig. S6(c,d). By applying voltage pulses of $> 0.8\,\mathrm{V}$ or $< -2.1\,\mathrm{V}$, the molecule could be switched between the two states. Because the 'up' and 'down' conformations have different adsorption sites (see Fig. S7), each switching is accompanied by a lateral displacement of the molecule. The STM-induced conformation change and lateral manipulation are effects of inelastic tunneling electrons that can excite molecular vibrations.[4]

In Fig. S6(e,f), LCPD maps of TTF-TDZ$_2$ in the 'up' and 'down' conformations are depicted. Both conformations show very similar LCPD contrast. Interestingly, the LCPD is increased above the entire molecule compared to the bare substrate, and the LCPD is increased above the positively charged donor part (center) compared to the negatively charged acceptor parts (ends). Again, this does not agree with the simple picture that the LCPD directly reflects the positive and negative partial charges of the molecule.

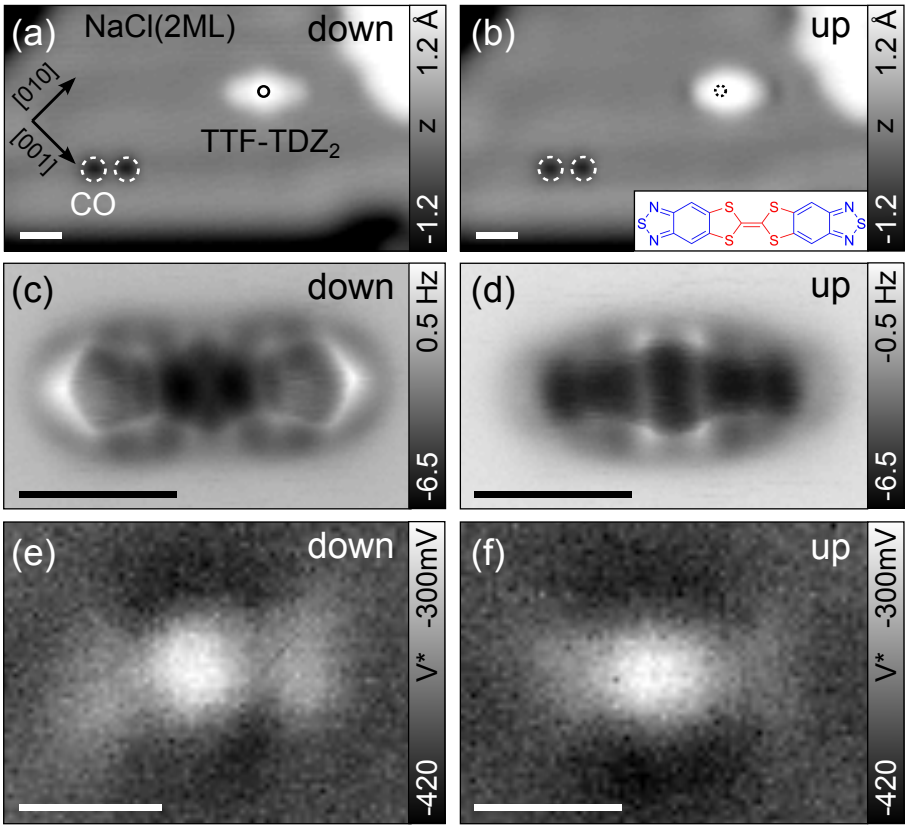

Figure S6: **TTF-TDZ$_2$ on NaCl(2ML)/Cu(111). (a,b)** Constant-current STM topographies ($I = 2\,\text{pA}$, $V = 0.2\,\text{V}$) of TTF-TDZ$_2$ in the 'down' (a) and 'up' (b) conformations recorded with a Cu tip. A voltage pulse of 0.8 V (at the position indicated by the black circle) was applied to switch between the conformations. A change in conformation is accompanied by a change in adsorption site from the TTF double bond on Cl top ('down') to a Cl bridge site ('up'). The inset in (b) shows the TTF-TDZ$_2$ structure with the donor part in red and the acceptor parts in blue. **(c,d)** Constant-height AFM images of TTF-TDZ$_2$ in the 'down' (c) and the 'up' (d) conformation, obtained with a CO tip. **(e,f)** LCPD (V^*) map of TTF-TDZ$_2$ in the 'down' (e) and the 'up' (f) conformation using a Cu tip. Scale bars: 10 Å.

Adsorption geometry and site

Both TTF-TDZ_2 and TTF-PYZ_2 adsorb in a boat geometry on NaCl(2ML)/Cu(111) with C_{2v} symmetry. In Fig. S7(a), the calculated[5] energy profile of the free (i.e. without substrate) TTF-PYZ_2 molecule as a function of the dihedral angle θ is plotted. For the free molecule, we find an optimal angle of $\theta = 12°$ with a rather small energy barrier for the flapping between the 'up' and 'down' conformations of 4 mV. On the surface TTF-TDZ_2 'down' ('up') adsorbs in the polar NaCl direction with the TTF double bond on Cl top (Cl bridge) as illustrated in Fig. S7(b,c). TTF-PYZ_2 'down' ('up') adsorbs in the polar (apolar) NaCl direction with the TTF double bond on Cl top (Cl bridge) as illustrated in Fig. S7(d,e). The adsorption sites were deduced from variable constant-height AFM images [see Fig. S7(f,g)].[6] Interestingly, both molecules in the 'down' conformation are adsorbed with their sulfur atoms of TTF on top of Na sites. This can be explained by the attractive interaction between the Na^+ ions and the lone pair of the sulfur atoms.[7] Note that for TTF-PYZ_2 the molecule conformations could not be switched because they are restricted to different substrate directions. However, the molecules could be manipulated laterally with similar voltage pulses as TTF-TDZ_2 but without changing the adsorption site or the conformation. This is indicative of the common TTF part being decisive for the molecule hopping on NaCl, probably through excitation of the TTF flapping mode by inelastic tunneling electrons.

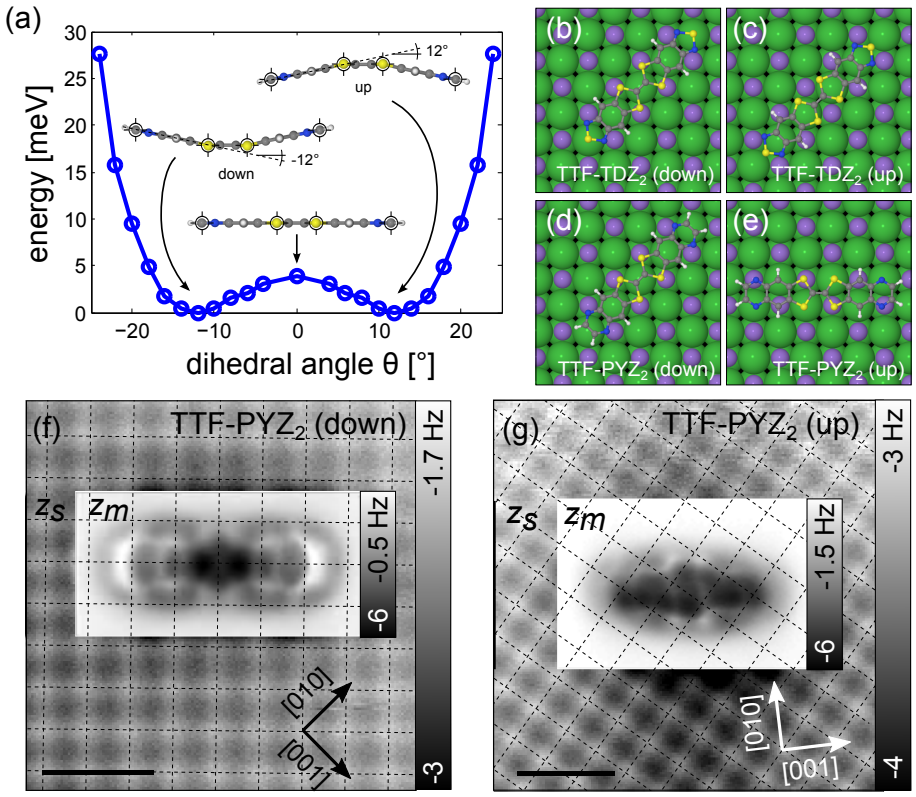

Figure S7: **Adsorption geometry.** **(a)** Calculated energy profile for the dihedral bending at the four sulfur atoms of TTF-PYZ_2. The ground-state energy of the molecule is set to zero. The dihedral angle θ between the atoms marked by black cross-hairs was fixed in the calculations. **(b/c)** Model of the experimental adsorption site for TTF-TDZ_2 in the 'down'/'up' conformations. **(d/e)** Model of the experimental adsorption site for TTF-PYZ_2 in the 'down'/'up' conformation. Color code: H: white, C: gray, N: blue, Na^+: purple, S: yellow, Cl^-: green. **(f,g)** Adjusted constant-height image of TTF-PYZ_2 in the 'down' (f) and 'up' (g) conformation with a CO tip (using two imaging heights, z_s and z_m). Note that for each imaging height, another contrast in Δf was chosen. The crossings of the dashed lines mark Cl atoms. Scale bars: 10 Å.

Synthesis of the Charge-transfer complexes

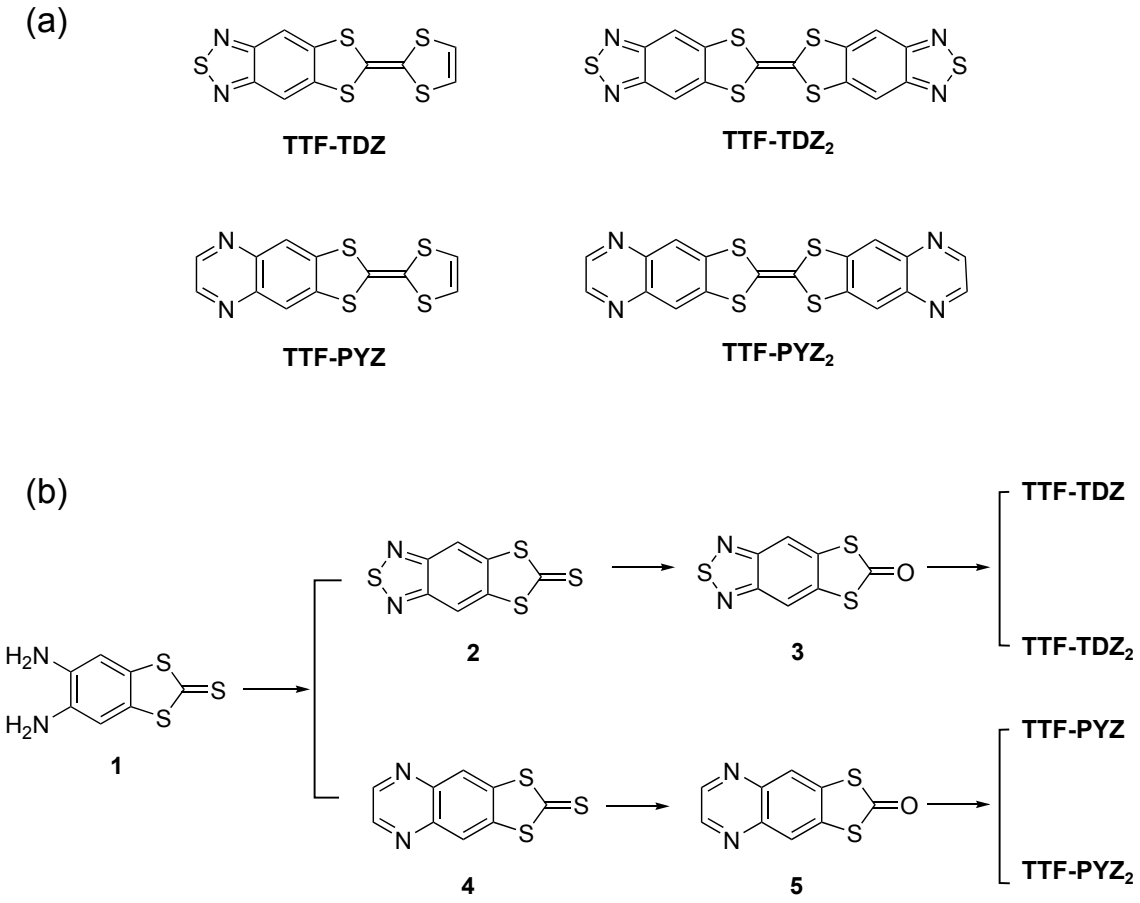

Scheme S1: **(a)** Molecule structures of **TTF-TDZ**, **TTF-TDZ$_2$**, **TTF-PYZ** and **TTF-PYZ$_2$**. **(b)** Synthetic route to obtain molecules in (a).

Unless stated otherwise, all reagents were purchased from commercial sources and used without additional purification, 6-(1,3-dithiol-2-ylidene)[1,3]dithiolo[4,5-*f*][2,1,3]benzothiadiazole (**TTF-TDZ**),[8] 5,6-diamino-1,3-benzodithiole-2-thione (**1**),[9–12] [1,3]dithiolo[4,5-*f*]-2,1,3-benzothiadiazole-6-thione (**2**),[13] [1,3]dithiolo[4,5-*f*]-2,1,3-benzothiadiazole-6-one (**3**)[8] and [1,3]dithiolo[4,5-*g*]quinoxaline-2-thione (**5**)[14] were prepared according to literature procedures.

6-([1,3]Dithiolo[4,5-*f*][2,1,3]benzothiadiazol-6-ylidene)[1,3]dithiolo[4,5-*f*][2,1,3]benzothiadiazole (**TTF-TDZ$_2$**):[15]

Triethyl phosphite (4 mL) was added to a solution of **3** (102 mg, 0.45 mmol) in toluene (2 mL)

under Ar. The mixture was refluxed for 3 h. After cooling to room temperature, the red solid was collected by filtration and washed with MeOH to afford **TTF-TDZ$_2$**.
Yield: 82 mg (87%); m.p. >350 °C; IR (KBr): ν = 3437, 2918, 1635, 1427, 1242, 1076, 839, 812, 800, 779, 635 cm^{-1}; ^{1}H and ^{13}NMR are unavailable because of its poor solubility; HRMS (ESI): m/z calcd for $C_{14}H_4N_4S_6$: 419.8755; found: 419.8755; elemental analysis calcd (%) for $C_{14}H_4N_4S_6$: C 39.98, H 0.96, N 13.32; found: C 39.86, H 1.11, N 12.82.

[1,3]Dithiolo[4,5-*g*]quinoxaline-2-one (**5**):
$Hg(OAc)_2$ (236 mg, 1 mmol) was added to a solution of **4** (1.6 g, 5 mmol) in dichloromethane (20 mL). The mixture was stirred at room temperature for 30 min. The light-yellow solid was filtered off while the filtrate was evaporated under reduced pressure to afford **5** as a white solid. Yield: 160 mg (73%); m.p. 262-263 °C; IR (KBr): ν = 3436, 3065, 1739, 1664, 1456, 1358, 1297, 1179, 1021, 931, 900, 868 cm^{-1}; ^{1}H NMR (300 MHz, DMSO-d_6): δ = 8.97 (s), 8.64 (s) ppm; ^{13}C NMR (75.5 MHz, DMSO-d_6): δ = 190.1, 146.2, 140.6, 135.2, 123.6 ppm. HRMS (ESI): m/z calcd for $C_9H_5N_2S_2$: 220.9838; found: 220.9838; elemental analysis calcd (%) for $C_9H_4N_2OS_2$: C 49.07, H 1.83, N 12,72; found: C 49.29, H 2.03, N 12.31.

2-(1,3-Dithiol-2-ylidene)[1,3]dithiolo[4,5-*g*]quinoxaline (**TTF-PYZ**):
Triethyl phosphite (8 mL) was added to a solution of **5** (440 mg, 2 mmol) and vinylene trithiocarbonate (537 mg, 4 mmol) in toluene (20 mL) under Ar. The mixture was refluxed for 3 h. After cooling to room temperature, followed by removal of toluene, the residue was purified by chromatography on silica gel initially eluting with hexane to remove excess triethyl phosphate, and then with a mixture of dichloromethane/THF = 1:1 to afford **TTF-PYZ** as a red solid. Yield: 240 mg (39%); m.p.: 253-254 °C; IR (KBr): ν = 3435, 3037, 1630, 1451, 1419, 1349, 1331, 1269, 1167, 1092, 1022, 963, 925, 881, 793, 779, 670 cm^{-1}; ^{1}H NMR 300 MHz, DMSO-d_6): δ = 8.81 (s), 8.21 (s), 6.82 (s); ^{13}C NMR (75.5 MHz, DMSO-d_6) δ = 145.4, 141.2, 141.0, 120.8, 119.9, 118.3, 103.2 ppm; HRMS (ESI): m/z calcd for $C_{12}H_6N_2S_4$:

305.9414; found: 305.9408.

2-([1,3]Dithiolo[4,5-*g*]quinoxalin-2-ylidene)[1,3]dithiolo[4,5-*g*]quinoxaline (**TTF-PYZ$_2$**): Triethyl phosphite (8 mL) was added to a solution of **5** (220 mg, 0.5 mmol) in toluene (4 mL) under Ar. The mixture was refluxed for 3 h. After cooling to room temperature, the red solid was collected by filtration and washed with MeOH to afford **TTF-PYZ$_2$**. Yield: 150 mg (74%); m.p. >350 °C; IR (KBr): ν = 3434, 3045, 1634, 1453, 1420, 1349, 1171, 1092, 1030, 978, 924, 881, 780, 683 cm^{-1}; ^{1}H NMR and ^{13}C NMR are unavailable because of its poor solubility; HRMS (ESI): m/z calcd for $C_{18}H_8N_4S_4$: 408.9705; found: 408.9699; elemental analysis calcd (%) for $C_{18}H_8N_4S_4$: C 52.92, H 1.97, N 13.71; found: C 52.81, H 1.89, N 13.27.

Spectroscopic characterization

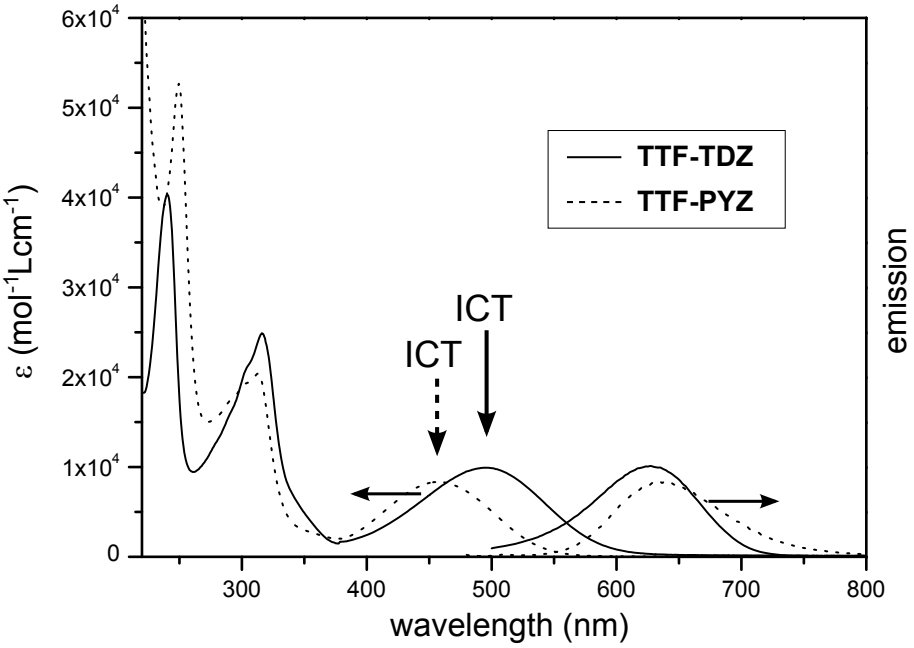

Figure S8: Absorption and emission spectra of **TTF-TDZ** (λ_{ex} = 460 nm , solid line) and **TTF-PYZ** (λ_{ex} = 450 nm , dotted line) in THF solution at room temperature. The vertical arrows mark the peaks of the absorption bands (λ_{abs}) corresponding to the intramolecular charge-transfer transition (ICT) of TTF-TDZ and TTF-PYZ, respectively.

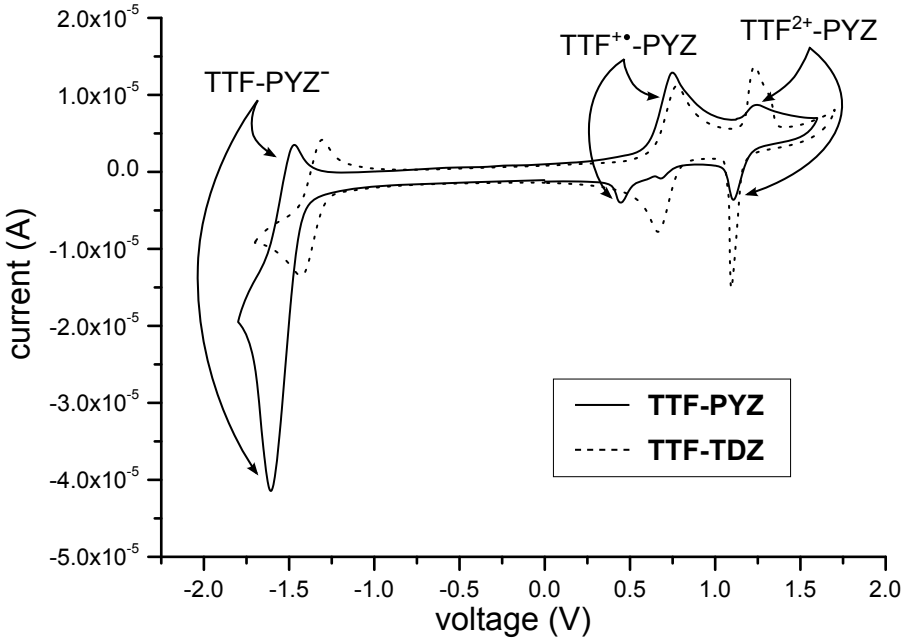

Figure S9: Cyclic voltammograms of **TTF-TDZ** (dotted line) and **TTF-PYZ** (solid line), recorded in DCM with ${}^{n}Bu_4NPF_6$ (0.1 mol dm^{-3}) as the supporting electrolyte.

The optical absorption spectra of **TTF-TDZ** and **TTF-PYZ** are shown in Fig. S8, and correspondingly Tab. S1 lists some selected data. Both compounds exhibit an analogous absorption profile that can be characterized by intense absorption bands at wavelengths below 350 nm. These high-energy absorptions can be assigned to $\pi\pi^*$ transitions, which are mainly localized on the donor and acceptor moieties. The broad and intense absorption band in the visible spectral region (above 400 nm) is typical for fused D-π-A molecules and essentially corresponds to an intramolecular charge-transfer transition (ICT), i.e., a one-electron excitation from the HOMO localized on the TTF unit to the LUMO localized on the acceptor moiety. Both compounds exhibit a weak fluorescence in the red part of the spectral region.

The electrochemical properties of **TTF-TDZ** and **TTF-PYZ** were investigated by cyclic voltammetry (Fig. S9 and Tab. S1). Both compounds show two oxidation waves, thus they can be oxidized to the radical ($TTF^{+\bullet}$-TDZ/PYZ) cation and dication (TTF^{++}-TDZ/PYZ) states sequentially and reversibly. In addition, both compounds exhibit one reversible reduction wave corresponding to the reduction of the acceptor moiety (TTF-TDZ^{-}/PYZ^{-}).

Table S1: Optical and electrochemical data, HOMO and LUMO energy levels of **TTF-TDZ** and **TTF-PYZ**.

	λ_{abs} (nm) (ϵ_{max} (10^4 $M^{-1}cm^{-1}$))	λ_{em} (nm)	$E_{g,opt}$(eV)[16]	E(V)[17]	HOMO(eV)[18]	LUMO (eV)[19]
TTF-TDZ	495 (0.99)	625	2.21	-1.84	-4.98	-3.02
TTF-PYZ	457 (0.83)	635	2.25	-2.02	-4.92	-2.9

Importantly, for both compounds, the electrochemical HOMO-LUMO gap matches fairly well with the optical HOMO-LUMO gap (taken from the crossing-point of the absorption and emission spectra).

Methods

Air- and/or water-sensitive reactions were conducted under Ar in dry, freshly distilled solvents. Elemental analyses were performed on an EA 1110 Elemental Analyzer CHN Carlo Erba Instruments. ^{1}H NMR spectra were recorded on a Bruker Avance 300 (300 MHz) spectrometer. Chemical shifts are reported in parts per million (ppm) and are referenced to the residual solvent peak (DMSO-d_6, ^{1}H = 2.50 ppm, ^{13}C = 39.52 ppm). The resonance labeled as (s) represents a single peak. FT-IR spectra were recorded on a Perkin Elmer One FT-IR spectrometer. High-resolution mass spectra were recorded with ESI (electrospray ionization) on a Thermo Scientific LTQ Orbitrap XL in the positive mode. The melting point was measured with Büchi B-540 microscope apparatus. Optical absorption spectra were recorded on a Perkin Elmer Lambda 900 UV/Vis/NIR spectrometer. Emission spectra were recorded on a Perkin Elmer LS 50B. Cyclic voltammetry was performed in a three-electrode cell equipped with a Pt-disk working electrode and a glassy carbon counter-electrode; an Ag/AgCl containing 2M LiCl (in ethanol) was used as reference electrode. The electrochemical experiments were carried out at room temperature under argon in dichloromethane (DCM) with $Bu_4N(PF_6)$ (0.1 M) as a supporting electrolyte. The voltammograms were recorded on a PGSTAT 101 potentiostat.

Notes and References

(1) Gross, L.; Mohn, F.; Moll, N.; Liljeroth, P.; Meyer, G. *Science* **2009**, *325*, 1110–1114.

(2) Gross, L.; Mohn, F.; Moll, N.; Schuler, B.; Criado, A.; Guitián, E.; Peña, D.; Gourdon, A.; Meyer, G. *Science* **2012**, *337*, 1326–1329.

(3) Bocquet, F.; Nony, L.; Loppacher, C.; Glatzel, T. *Phys. Rev. B* **2008**, *78*, 035410.

(4) Swart, I.; Sonnleitner, T.; Niedenführ, J.; Repp, J. *Nano Lett.* **2012**, *12*, 1070–1074.

(5) The DFT calculations were performed with the `CPMD` code (see main text for details).

(6) Schuler, B.; Liu, W.; Tkatchenko, A.; Moll, N.; Meyer, G.; Mistry, A.; Fox, D.; Gross, L. *Phys. Rev. Lett.* **2013**, *111*, 106103.

(7) Pavliček, N.; Fleury, B.; Neu, M.; Niedenführ, J.; Herranz-Lancho, C.; Ruben, M.; Repp, J. *Phys. Rev. Lett.* **2012**, *108*, 086101.

(8) Geng, Y.; Pfattner, R.; Campos, A.; Hauser, J.; Laukhin, V.; Puigdollers, J.; Veciana, J.; Mas-Torrent, M.; Rovira, C.; Decurtins, S.; Liu, S.-X. *Chem. Eur. J.* **2014**, (in press).

(9) Jia, C.; Liu, S.-X.; Tanner, C.; Leiggener, C.; Sanguinet, L.; Levillain, E.; Leutwyler, S.; Hauser, A.; Decurtins, S. *Chem. Commun.* **2006**, 1878–1880.

(10) Jia, C.; Liu, S.-X.; Tanner, C.; Leiggener, C.; Neels, A.; Sanguinet, L.; Levillain, E.; Leutwyler, S.; Hauser, A.; Decurtins, S. *Chem. Eur. J.* **2007**, *13*, 3804–3812.

(11) Goze, C.; Dupont, N.; Beitler, E.; Leiggener, C.; Jia, H.; Monbaron, P.; Liu, S.-X.; Neels, A.; Hauser, A.; Decurtins, S. *Inorg. Chem.* **2008**, *47*, 11010–11017.

(12) Jia, H.-P.; Liu, S.-X.; Sanguinet, L.; Levillain, E.; Decurtins, S. *J. Org. Chem.* **2009**, *74*, 5727–5729.

(13) Jia, H.-P.; Ding, J.; Ran, Y.-F.; Liu, S.-X.; Blum, C.; Petkova, I.; Hauser, A.; Decurtins, S. *Chem. Asian J.* **2011**, *6*, 3312–3321.

(14) Geng, Y.; Fiolka, C.; Krämer, K.; Hauser, J.; Laukhin, V.; Decurtins, S.; Liu, S.-X. *New J. Chem.* **2014**, *38*, 2052.

(15) Tucker, N. M.; Briseno, A. L.; Acton, O.; Yip, H.-L.; Ma, H.; Jenekhe, S. A.; Xia, Y.; Jen, A. K.-Y. *ACS Appl. Mater. Interfaces* **2013**, *5*, 2320–2324.

(16) The optical band gap is estimated from the cross point of UV-vis absorption and emission spectra.

(17) The reduction potentials vs. Fc^+/Fc were recorded in CH_2Cl_2-Bu_4NPF_6 (0.1 M) solution.

(18) The HOMO level is calculated from the onset of the first oxidation potential in cyclic voltammetry according to the equation $E_{\mathrm{HOMO}} = [-e(E^{\mathrm{ox}}_{\mathrm{onset}} + 4.8)]$ eV, where 4.8 eV is the energy level of ferrocene below the vacuum level.

(19) The LUMO level is calculated from the onset of the first reduction potential in cyclic voltammetry using the equation $E_{\mathrm{LUMO}} = [-e(E^{\mathrm{red}}_{\mathrm{onset}} + 4.8)]$ eV, where 4.8 eV is the energy level of ferrocene below the vacuum level.